D4.7 Upgrade of X-ray imaging system to provide 3D features based on 2D scanners ready for integration.

Fresh and processed food production line

Mattias van Dael, Pieter Verboven

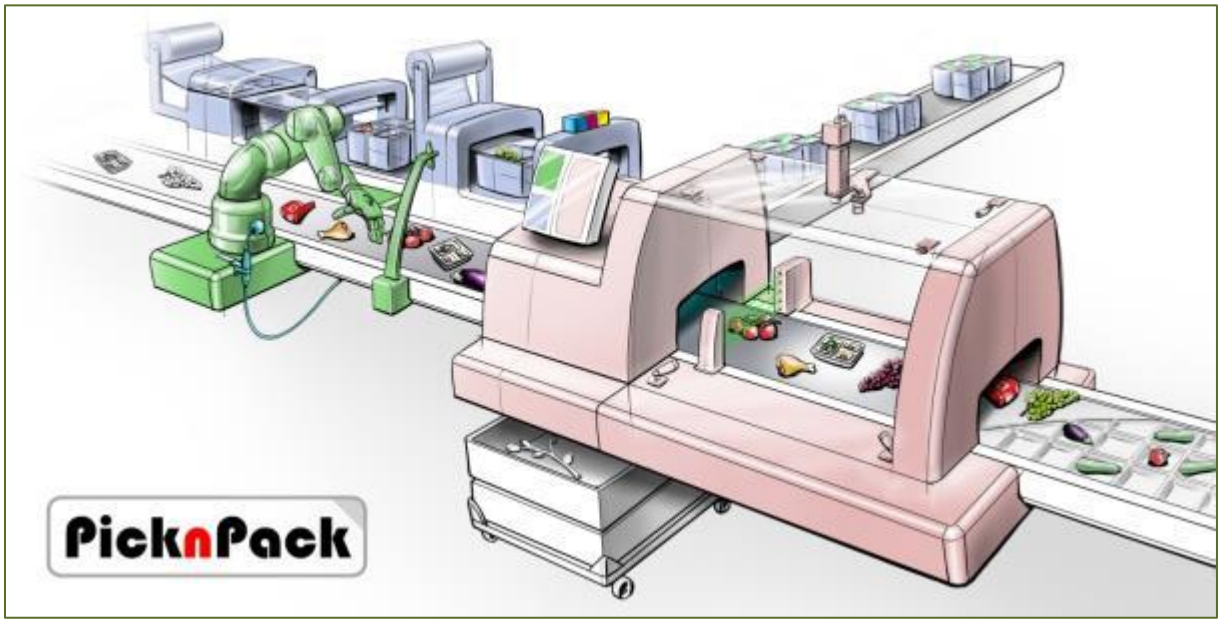

Flexible robotic systems for automated adaptive packaging of fresh and processed food products

The research leading to these results has received funding from the European Union Seventh Framework Programme under grant agreement n° 311987.

Dissemination level		
PU	Public	X
PR	Restricted to other programme participants (including the EC Services)	
RE	Restricted to a group specified by the consortium (including the EC Services)	
CO	Confidential, only for members of the consortium (including the EC Services)	

Table of Contents

1 Introduction

X-ray radiographs allow for inspection of internal quality, but do not provide 3Dimensional information in the same way for example computed tomography (CT) does. Here, stereoscopy is used to derive the 3Dimensional location of a feature by using a X-ray radiograph scanner with two source-detector pairs with a relative angle of 50°.

2 X-ray imaging hardware

The X-ray imaging module is equipped with dual source-detector pairs as shown in Figure 1. The image on the left shows a rendering of the complete module, with the two X-ray beams in green. The middle image shows a photograph of the sources, while the right photograph shows the detectors as seen through the tunnel without a conveyor belt or transport system installed. The detectors are located next to each other underneath the web of packages, to allow to stop the transport system in between packages during the stop and go motion, to minimize missing data.

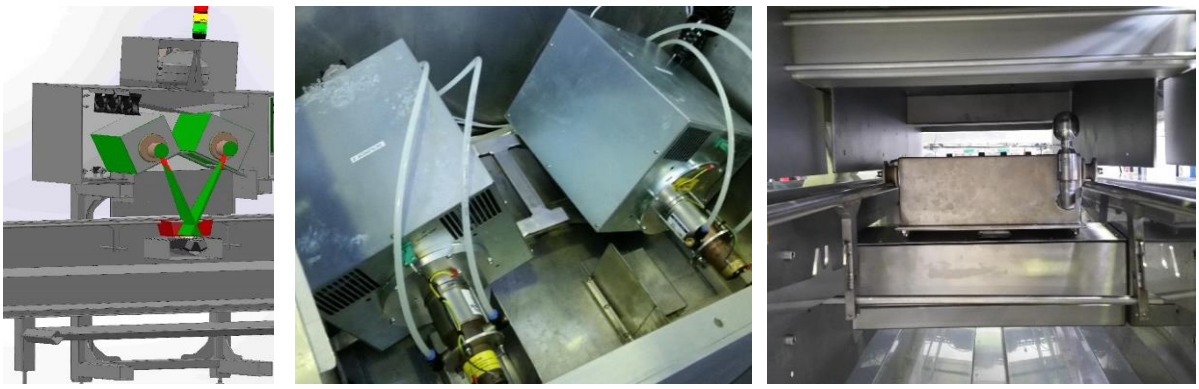

Figure 1: Setup of the dual source-detectors pair in the X-ray imaging module.

The optimal stereo angle was determined by simulating radiographs using the ASTRA toolbox [1], [2] for different setups, as shown in Figure 2. Phantoms were created for both tomato trusses and completely filled trays. The optimal angle was determined to be 50° between both source-detector axis (25° w.r.t. the vertical) to avoid tray overlaps.

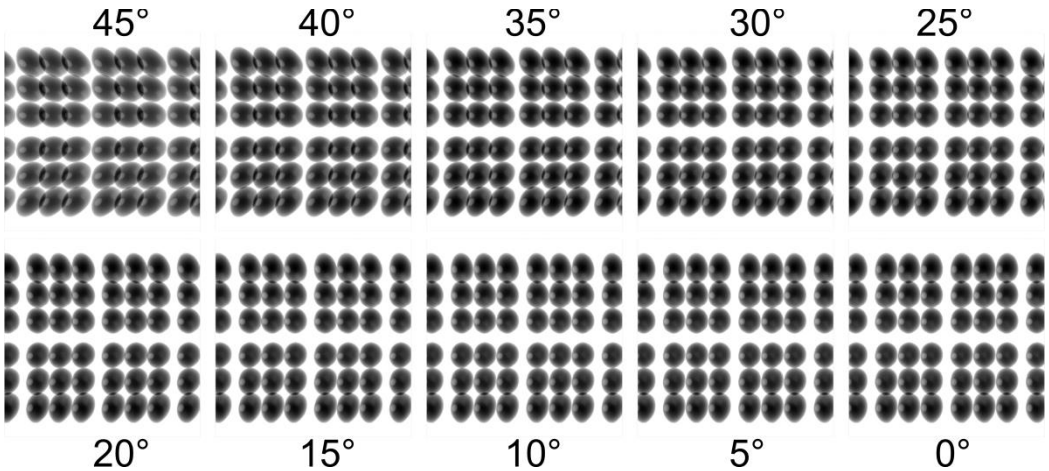

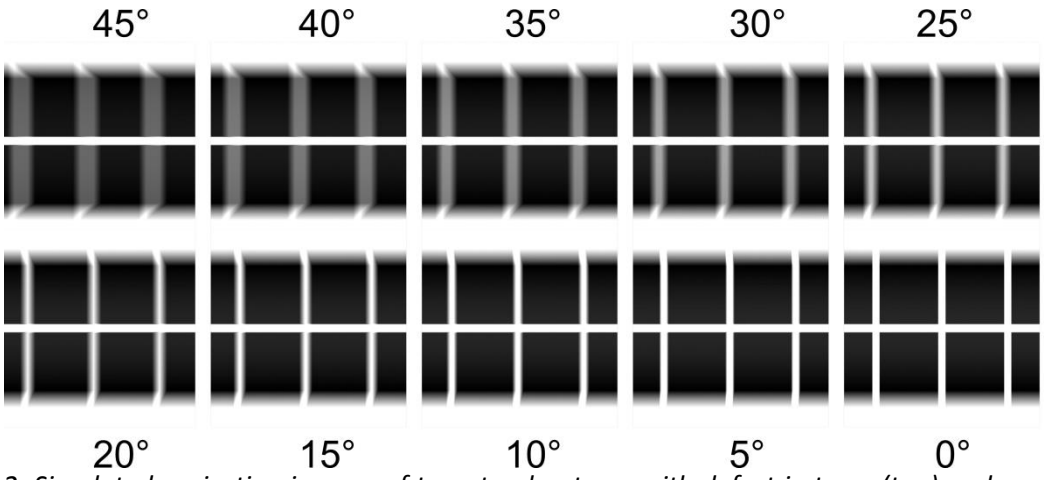

Figure 2: Simulated projection images of tomato phantoms with defect in trays (top) and completely filled trays (bottom) with the angle of the source-detector axis (α) ranging from 45 to 0° w.r.t. the vertical.

3 3D feature localization through stereoscopy

The stereo setup has two main advantages. Firstly, it provides multiple views of the sample allowing to distinguish features that are located along one of the source-detector axes and occlude each other in the resulting projection (Figure 3). They can easily be distinguished in the second projection from a different viewpoint though.

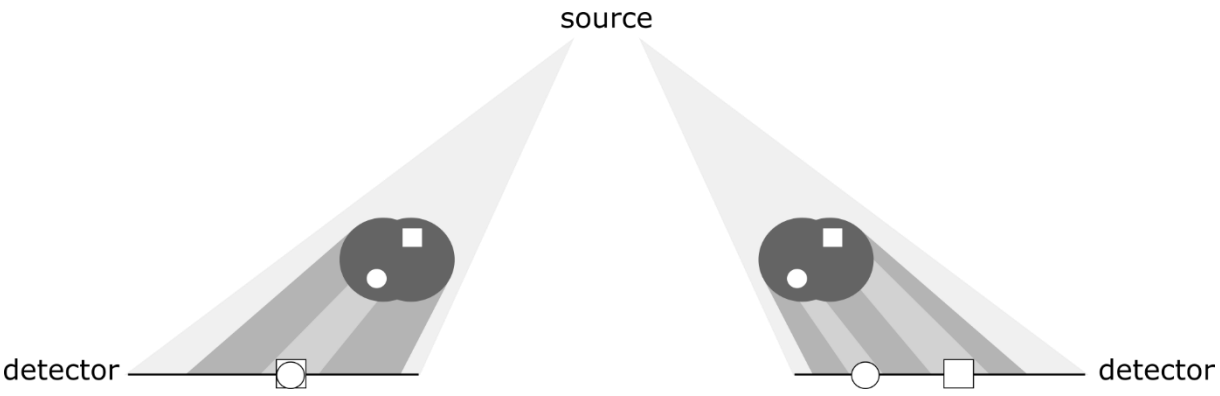

Figure 3: Taking multiple views of the same object provides the possibility to distinguish defects that are occluded in a single view.

Secondly, features identified in both radiographs can be placed in 3Dimensional space using stereoscopy. Stereoscopy is the process where depth information is extracted from image pairs taken from a slightly different angle, by determining the displacement of the feature in the image pair. Consider a sample with two defects as seen in Figure 4. The sample is imaged from two different viewpoints. Notice that the position of the two defects in the projections is switched, because of their different locations along the height of the sample, an effect called parallax displacement. Measuring this displacement and combining it with the known geometry of the imaging systems allows us to accurately determine the vertical position of the defects using simple trigonometry.

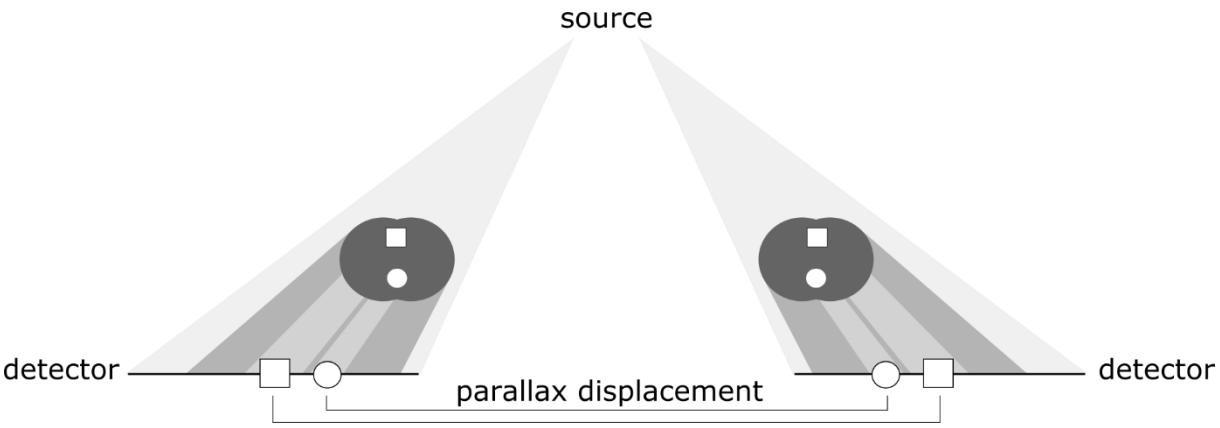

Figure 4: Parallax displacement of two defects in a sample imaged from two different viewpoints, resulting in a parallax displacement of the defect in the eventual images as projected on the detectors.

4 Multi-sensor inspection

4.1. Defect detection

A new method is proposed that explicitly takes into account the shape, size and orientation of the object by means of a 3D vision system and a deformable shape model. The principle of the method is demonstrated by comparing it to radiography detection algorithms which use a conventional method of imaging and detection.

To detect internal defects, the radiograph of a sample that is captured by the X-ray detector is compared with a radiograph that is simulated from a reference object free of defects. The reference object is determined by fitting a deformable shape model to the surface point cloud obtained by a 3D vision system with the same density distribution of the agrofood product that is to be inspected.

Step 1. Shape model fitting

The proposed method requires the surface shapes of the population of samples to be known in the form of a deformable shape model [3]. During inspection this deformable shape model is fitted to the point cloud measured by a 3D vision system. To simplify the fitting process, a principal component analysis (PCA) based shape model is used. The model is constructed a priori for the population of agrofood products (such as the pears under study in this document) subject to inspection by a manual alignment, determining the outer shape, finding corresponding points by interpolating to a grid in a spherical coordinate system and applying a PCA to their coordinates for a number of product items. This results in a mean position for every point, representing the mean shape, and displacement vectors for every point represented by the principal, or shape, components [4]. Any shape originating from the same population as from which the deformable model was built can be represented as a linear combination of the mean shape and the shape components as shown in Eq. 1.

$$C = Sw + \mu \qquad (1)$$

In Eq. 1, $\mathbf{C}$ is containing the 3D coordinates of the *n* points describing the shape. $\mathbf{S}$ is the *n*-by-*s* matrix containing the shape components or displacement from the mean vectors with *s* being the number of components used to create the shape model. The weight of each components is contained in $\mathbf{w}$. The matrix $\boldsymbol{\mu}$ contains the 3Dimensional coordinates of the *n* points describing the mean model shape.

The shape model is fitted to the measured surface point cloud obtained by the (virtual) 3D vision system. Various methods have been described in literature to register deformable shape models to unstructured point clouds. In this work an iterative closest point (ICP) registration [5] is followed by a least squares based fit of each model vertex to the closest measured point. A least squares approach is possible in the case of PCA-based models where any shape can be described as a linear combination of the mean shape and the shape components (Eq. 1). The system is solved iteratively until convergence is reached, resulting in a transformation matrix describing the shape model's pose and a matrix $\mathbf{w}$ containing the shape components weights, as described in Eq. 1. Figure 5 shows a pear shape model fitted against three different point clouds and bar charts displaying the weights of the first 15 model components explaining 99% of variance.

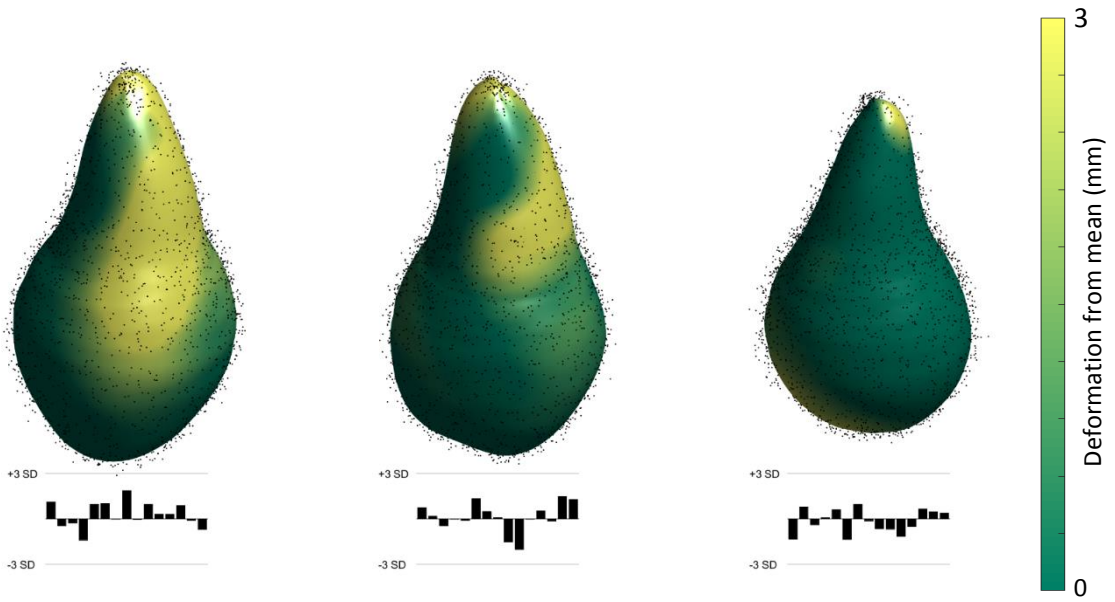

Figure 5: A pear shape model fitted to 3 different point clouds, color scale indicates the model deformation from the mean. Below, bar charts display the weights of the first 15 components expressed in standard deviations, together explaining 99% of the model variance.

Step 2. X-ray simulation

The ASTRA toolbox is used to generate a simulated radiograph without defects of the fitted shape obtained in step 1. To achieve a radiograph that can be compared with the measured one, the following aspects need to be taken into account.

First, the fitted shape needs to be converted from a surface mesh to a volumetric representation, a process called voxelization as shown in Figure 6. This volumetric representation is equivalent to a 3Dimensional image, where each voxel value (a voxel is the 3Dimensional equivalent of a pixel) represents the local sample density which is in this case proportional to the local X-ray linear attenuation coefficient, The latter is the actual output of a full CT-scan. Voxelization of the shape model, which essentially is a set of point coordinates and the facets connecting them, is carried out by a ray intersection algorithm as described by Patil and Ravi (2005). It passes rays along the X-axis in a preset order (incremented along the Y-axis first, then along the Z-axis). If the shape model is error-free, i.e., a closed, non-selfintersecting surface, the number of intersections of each ray with the model is even. Voxels along the ray between an odd and the next even intersection are considered to be inside the model and are thus filled. This process is repeated along the Y and Z axis to minimize errors. For now, the internal density distribution is assumed to be uniform, i.e., all voxels will assume the same value. Future work will include non-uniform density distributions.

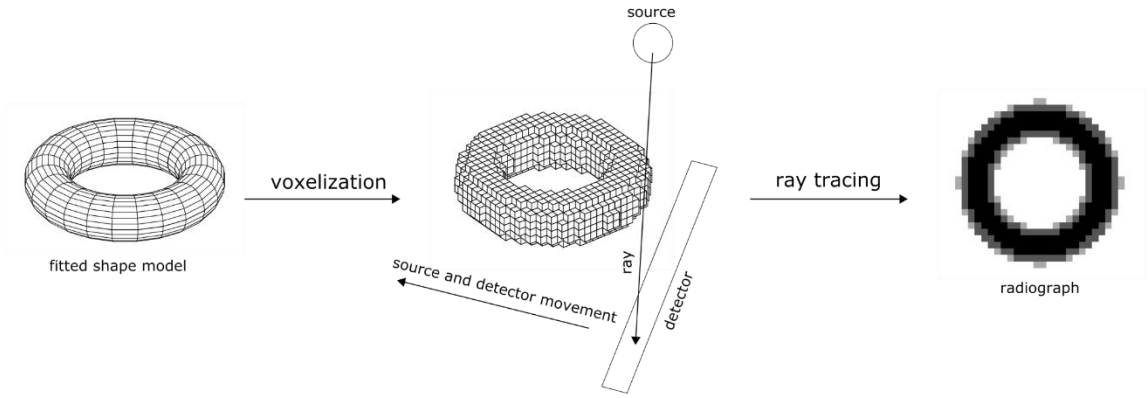

Figure 6: Workflow to simulate a radiograph from a shape model. The fitted shape model is converted to a voxel-representation using a ray-intersection algorithm. This is then used to generate a radiograph using the appropriate geometric properties.

Second, the scanner geometry and properties have to be known to facilitate an exact comparison between measured and simulated radiographs. To simulate a cone-beam geometry the ASTRA-toolbox requires the source and detector position as well as the detector and pixel size, as shown in Figure 6. The sample object is assumed to be centered in the coordinate system origin. The majority of industrial X-ray radiograph scanners are line scanners, i.e. the detector size is 1 pixel in the direction of movement. During simulation the sample remains in the origin but source and detector move in the opposite conveyor direction over a distance equal to the detector pixel size. The resulting 1-pixel wide projections images are stitched together to form a complete radiograph. In this study, the source and detector were assumed to be 500 mm above and 50 mm below the conveyor respectively, while the detector was assumed to have a width of 200 mm. To study the effect of pixel size on detection accuracy, radiographs were simulated for pixel sizes of 0.5, 1 and 2 mm.

To obtain a radiograph using these parameters, a ray-tracing algorithm is used within the ASTRA toolbox, where a ray is defined as one of the lines connecting the source with an individual detector pixel. The ASTRA toolbox uses a GPU implementation of the slice-interpolated projection scheme [1], [7] which uses bilinear interpolation within each slice and integrates the results in a trapezoidal fashion along each ray.

Step 3. Comparison of radiographs

Comparing measured and simulated radiographs can be done in several ways. Standardized methods such as the structural similarity index (SSIM, Wang et al., 2004, 2003), histogram comparison [10] and Fourier ring correlation [11] are available to assess similarity. In this work, a different approach was used. Because the two radiographs are taken from the same product orientation it is straightforward to simply subtract them to obtain a residual image. From this image one or multiple features can be determined to be used in a classic classification process. Differences between the radiographs will be present as positive or negative pixel values in the residual image. Some differences might be present here that are not linked to the presence of any defects due to errors in the algorithm, mostly due to misalignment and resampling differences during voxelization. It makes sense to choose a feature that results in a net difference measure so that small, random errors due to the reason described above and sensor noise which are both zero-centered are canceled out. The simplest feature possessing this property is the sum over all residual pixels, and is used in what follows as classification feature. This feature is fed into a 10-fold cross-validated naive Bayesian classifier [12].

4.2. Reference detection methods

Reference classification methods using only X-ray radiography were used to evaluate the performance of the proposed method.

Firstly, human operators were used as reference. A GUI was developed that presented the human operators with the 2240 radiographs of torus samples in random order. For each of these the operators could indicate whether they could visually determine if a defect was present or not. This process was repeated for the different detector resolutions.

Secondly, defects were segmented from simulated radiographs (Figure 7) by applying a local adaptive threshold as described in Figure 7. False positives generated by the sample edge were removed with a mask generated by dilating the Otsu-thresholded [13] projection (Figure 7c and d). After removing pixels without neighbors, the summed area of the remaining blobs was fed into a 10-fold cross-validated naive Bayesian classifier.

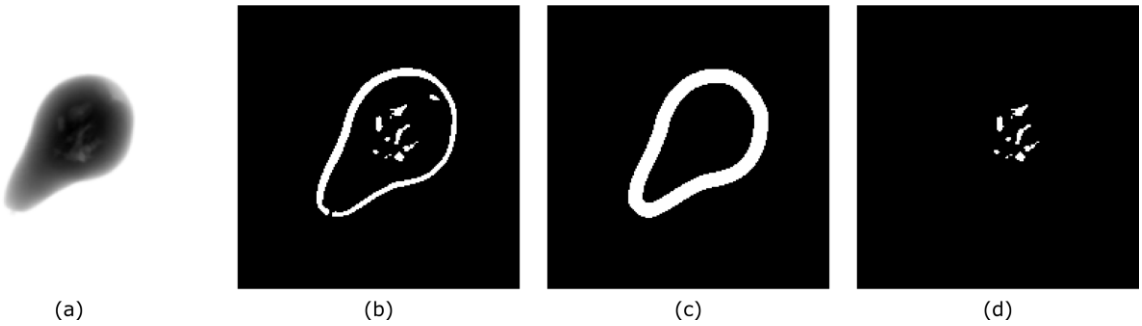

Figure 7: Steps in the reference defect detection method for pears using X-ray radiography. (a) shows a random radiograph, (b) shows the result of the local adaptive threshold, (c) shows the edge mask, (d) is the result of subtracting (c) from (b) and shows the segmented defect.

4.3. Results

Results show that the proposed method is more accurate than the reference methods in detecting small defects with a limited density deviation and on par with the reference methods in detecting large cavities. Also, the proposed method has a higher positive predictive value, meaning the end product is on average of higher quality. Additionally, it should be noted not many improvements can be made to the reference methods, while several improvements have been proposed to increase the proposed method's performance. Combined with the fact that the proposed method detects deviations from the ideal and is not focused on detecting specific defects or features this shows that the proposed method is a very promising technology. The method has been submitted as patent application PCT/EP2016/055718 "AUTOMATED QUALITY CONTROL AND SELECTION".

5. References

[1] W. J. Palenstijn, K. J. Batenburg, and J. Sijbers, "Performance improvements for iterative electron tomography reconstruction using graphics processing units (GPUs).," *J. Struct. Biol.*, vol. 176, no. 2, pp. 250–3, Nov. 2011.

[2] W. van Aarle, W. J. Palenstijn, J. De Beenhouwer, T. Altantzis, S. Bals, K. J. Batenburg, and J. Sijbers, "The ASTRA Toolbox: A platform for advanced algorithm development in electron tomography," *Ultramicroscopy*, vol. 157, pp. 35–47, 2015.

[3] D. C. Schneider and P. Eisert, "Fitting a morphable model to pose and shape of a point cloud," in *Vision, Modeling, and Visualization Workshop 2009. Proceedings*, 2009, pp. 93–100.

[4] F. Danckaers, T. Huysmans, M. van Dael, P. Verboven, B. Nicolai, and J. Sijbers, "Building a statistical shape model of the apple from corresponded surfaces.," *Chem. Eng. Trans.*, vol. 44, pp. 49–54, 2015.

[5] P. J. Besl and H. D. McKay, "A method for registration of 3D shapes," *IEEE Trans. Pattern Anal. Mach. Intell.*, vol. 14, no. 2, pp. 239–256, 1992.

[6] S. Patil and B. Ravi, "Voxel-based Representation, Display and Thickness Analysis of Intricate Shapes," in *Ninth International Conference on Computer Aided Design and Computer Graphics (CAD-CG'05)*, 2005, pp. 415–422.

[7] F. Fang Xu and K. Mueller, “A Comparative Study of Popular Interpolation and Integration Methods for Use in Computed Tomography,” in *3rd IEEE International Symposium on Biomedical Imaging: Macro to Nano, 2006.*, 2006, pp. 1252–1255.

[8] Z. Wang, E. P. Simoncelli, and A. C. Bovik, “Multiscale structural similarity for image quality assessment,” in *The Thrity-Seventh Asilomar Conference on Signals, Systems & Computers, 2003*, 2003, vol. 2, pp. 1398–1402.

[9] Z. Wang, A. C. Bovik, H. R. Sheikh, and E. P. Simoncelli, “Image Quality Assessment: From Error Visibility to Structural Similarity,” *IEEE Trans. Image Process.*, vol. 13, no. 4, pp. 600–612, Apr. 2004.

[10] Y. Cao and L. Petzold, “Accuracy limitations and the measurement of errors in the stochastic simulation of chemically reacting systems,” *J. Comput. Phys.*, vol. 212, no. 1, pp. 6–24, 2006.

[11] N. Banterle, K. H. Bui, E. A. Lemke, and M. Beck, “Fourier ring correlation as a resolution criterion for super-resolution microscopy,” *J. Struct. Biol.*, vol. 183, no. 3, pp. 363–367, 2013.

[12] K. Larsen, “Generalized Naive Bayes Classifiers,” *ACM SIGKDD Explor. Newsl.*, vol. 7, no. 1, pp. 76–81, Jun. 2005.

[13] N. Otsu, “A Threshold Selection Method from Gray-Level Histograms,” *IEEE Trans. Syst. Man. Cybern.*, vol. 9, no. 1, pp. 62–66, 1979.